Electrical properties of a *p–n* heterojunction of Li-doped NiO and Al-doped ZnO for thermoelectrics

Temesgen D. Desissa[†], Matthias Schrade[§], Truls Norby[†,*]

[†]*Department of Chemistry, Centre for Materials Science and Nanotechnology, University of Oslo, FERMiO, Gaustadalléen 21, NO-0349 Oslo, Norway*

[§]*Department of Physics, Centre for Materials Science and Nanotechnology, University of Oslo, FERMiO, Gaustadalléen 21, NO-0349 Oslo, Norway*

Abstract

The electrical properties of a *p–n* heterojunction of polycrystalline *p*-type $Ni_{0.98}Li_{0.02}O$ and *n*-type $Zn_{0.98}Al_{0.02}O$ have been investigated for potential applications in high-temperature oxide-based thermoelectric generators without metallic interconnects. Current-voltage characteristics of the junction were measured in a two-electrode setup in ambient air at 500 – 1000 °C. The resistance and rectification of the junction decreased with increasing temperature. A non-ideal Shockley diode model was used to fit the measured current-voltage data in order to extract characteristic parameters of the junction, such as area-specific series resistance R_s and parallel shunt resistance R_p, non-ideality factor, and the saturation current density. R_s and R_p decreased exponentially with temperature, with activation energies of 0.4 ± 0.1 eV and 1.1 ± 0.2 eV, respectively. The interface resistance of the direct *p–n* junction studied here is as such too high for practical applications in thermoelectrics. However, it is demonstrated that it can be reduced by order of magnitude by using a composite of the individual materials at the interface, yielding a large effective contact area.

Keywords: Li-doped NiO; Al-doped ZnO; *p–n* junction; composite; oxide thermoelectrics

[*] *Corresponding author, e-mail:* truls.norby@kjemi.uio.no

Introduction

Heat from renewable sources or waste heat from industries, municipalities, or transportation can be converted to electricity by thermoelectric generators (TEGs) based on the Seebeck effect [1]. Compared with state-of-the-art metallic thermoelectric materials [2], oxides are thermochemically more stable, generally less toxic, more abundant, and cheaper, but also less efficient [3]. Traditional TEGs consist of *p*- and *n*-type thermoelectric legs connected electrically in series and thermally in parallel. Metallic contact layers - so called interconnects - are used to ensure ohmicity of the contact and absorb mismatches in thermal expansion. However, these metallic layers complicate device fabrication and increase manufacturing cost, and tend to be troubled by interdiffusion, oxidation, and delamination. Interconnect-free module designs have been studied by Span *et al.*[4] and Becker *et al.* [5] for Si-based materials. In addition, Shin *et al.* have demonstrated a thermoelectric module with a direct contact between two oxide materials [6, 7].

In order to have a better foundation for evaluating and exploring direct oxide *p*–*n* junctions, we are studying different aspects of couples of *p*-type Li-doped NiO and *n*-type Al-doped ZnO, with band gaps of, respectively, ~ 3.7 eV and ~ 3.4 eV [8]. Li is an efficient acceptor dopant in NiO to increase the concentration of electron holes [9] while Al-doping correspondingly increases the concentration of electrons in ZnO [10].

Al-doped ZnO is among the best *n*-type oxides for thermoelectrics stable in air, with reported figure of merit, zT, as high as 0.5 at 1050 °C. The thermoelectric properties of Li-doped NiO, however, are less studied, but a maximum zT of 0.1 at 1000 °C has been reported. Detailed investigations of the thermoelectric properties of ZnO [11-13] and NiO [14, 15] can be found in the literature and are not within the scope of the current paper.

NiO and ZnO form, respectively, cubic and hexagonal structures with finite mutual solid solubility, without forming any intermediate compound according to the NiO-ZnO phase diagram [16, 17] from the chemical stability viewpoints. Thus, NiO and ZnO form a stable *p*–*n* junction, and for this we recently reported on the stability and cation inter-diffusion across the present heterojunction, i.e., $Ni_{0.98}Li_{0.02}O$–$Zn_{0.98}Al_{0.02}O$, in the temperature range 900–1200 °C [18].

Here we present an analysis of electrical properties of the heterojunction between polycrystalline $Ni_{0.98}Li_{0.02}O$ and $Zn_{0.98}Al_{0.02}O$. Furthermore, we demonstrate the reduction of the interfacial resistance by use of the high effective contact area of a composite interface layer.

Experimental procedure

$Ni_{0.98}Li_{0.02}O$ and $Zn_{0.98}Al_{0.02}O$ were synthesized via a standard solid-state method using high purity chemicals (≥ 99%) of Li_2CO_3 (Sigma-Aldrich), NiO (Fuel Cell Materials), Al_2O_3 (Sigma-Aldrich) and ZnO (Sigma-Aldrich). The appropriate amounts of the precursors were weighed and mixed by rotary ball milling for several hours. The Li-doped NiO precursor mixture was calcined at 900 °C for 6 h to decompose the Li_2CO_3, followed by manual grinding using mortar and pestle. The precursor mixtures were uniaxially pressed in a 10 mm diameter steel die (Specac, UK). The obtained green body pellets of Li-doped NiO and Al-doped ZnO were sintered at 1250 °C and 1350 °C, respectively, to reach final relative bulk densities > 98%. To prepare the composite sample (*c*), a 50/50 mol% mixture of Li-doped NiO and Al-doped ZnO was ball milled in isopropanol, dried, pressed into a pellet, and sintered at a lower temperature of 950 °C. Microstructural characterization of the sintered samples was carried out using field emission scanning electron microscopy (SEM) (Quanta FEG 200, FEI).

The faces of all pellets were ground and polished down to ¼ μm using diamond abrasive (DP-spray P, Struers, Denmark) before establishing the junctions. Platinum electrodes were painted on the

outer faces of the junction couples using platinum ink (METALOR) and contacted to instrumentation via 0.5 mm diameter Pt wires. The assemblies of wires and samples (*p*–*n* and *p*–*c*–*n* junctions) were held together by a spring-load system in a ProboStat™ measurement cell (NorECs, Norway). Current-voltage measurements were carried out in the temperature range 500 –1000 °C in ambient air. Agilent E3642A and 34970A instruments were used to supply a constant DC voltage and to measure the resulting current, respectively. Data acquisition was done by a custom-made LabVIEW software. Mott-Schottky capacitance-voltage (C-U_A) measurements were carried out on the heterojunction at 900 °C in ambient air using the same measurement cell but utilizing a potentiostat (Reference 600, Gamry) operating at a constant frequency of 1 MHz while applying various DC biases to the *p*–*n* junction. Onwards, unless otherwise noted, we report area-specific values for the resistances and currents by taking the area (0.8 cm^2) of the disks, electrodes, and junctions into account.

Results and discussions

Figure 1 shows characteristic curves of measured current density against applied voltage (j-U_A) of the $Ni_{0.98}Li_{0.02}O$ and $Zn_{0.98}Al_{0.02}O$ heterojunction in the temperature range 500 – 1000 °C. The junction is clearly rectifying at the lower temperatures, while the degree of rectification decreases with increasing temperature.

The electrical behavior of heterojunctions can often be described by the equivalent circuit schematically illustrated in the inset of *Figure 1* [19]. It consists of a series resistance (R_s) accounting for ohmic contribution of wires and bulk components, the diode element (D), and a parasitic parallel shunt resistance (R_p), which describes ohmic transport through the junction. The current-voltage characteristic can be related to those parameters of the equivalent circuit by the non-ideal Shockley diode model [19-22], which is given as

$$j = \left(\frac{R_p}{R_p+R_s}\right)\left\{j_0\left[\exp\left(\frac{e(U_A-jR_s)}{\eta_{id}k_BT}\right)-1\right]\right\}+\frac{U_A}{R_p} \quad (1)$$

Here, j is the total measured current density, j_0 the temperature dependent saturation current density, η_{id} the non-ideality factor, U_A the applied bias voltage, T the absolute temperature, and other symbols have their usual meanings. It may be noted that this is an implicit relation, as j appears on both sides of the equation, and it hence needs to be solved numerically. In most standard *p–n* junction solid-state devices operating at moderate temperatures, R_p is high and can be neglected. Eq. (1) then reduces to a simple R_s-corrected non-ideal diode equation [23]. However, in our investigation at high temperatures, both series and parallel parasitic resistances play a role, and the full equation will be used. The experimental data of *Figure 1* are fitted to equation (1) by varying the junction specific parameters R_s, R_p, j_0, and η_{id}, and the result is summarized in *Table I*.

At temperatures below 500 °C and in the reverse bias direction, the limiting resolution of the amperemeter used prevents a good fit to the model. Above 600 °C, however, the experimental data are well described by the fitted curves and hence by the model of equation (1).

The extracted non-ideality factor varies between about 2.5 at the lowest temperature and unity at the highest temperature. The relatively large non-ideality factor at low temperatures is reported also in earlier reports for NiO–ZnO systems [24, 25].

The saturation current density, j_0 increased from about 0.5 mA/cm^2 at 500 °C to about 30 mA/cm^2 at 900 °C. The dependence of j_0 on temperature can be written as [19, 26-28]

$$j_0 = j_{00}\exp\left(\frac{-E_a}{\eta_{id}k_BT}\right) \quad (2)$$

where, j_{00} is a temperature independent pre-exponential factor, E_a is an activation energy corresponding to excitation and transport of charge carriers, and the other parameters have their

usual meanings. A plot of ($\eta_{id} \log j_0$) against inverse temperature showed an activation energy E_a = 3.2 ± 0.2 eV, *Figure 2.* This activation energy is roughly similar to the average band gap of the *p*- and *n*-type materials, about 3.5 eV [8]. This indicates that the charge transport across the junction may be dominated by diffusion of minority carriers at high temperatures contributing to the saturation current density [29], in contrast to a widely reported recombination limited transport process at ambient temperatures [24, 25, 30].

Figure 3 shows an Arrhenius plot of resistances R_s and R_p. The bends towards lower resistances above 900 °C may be speculated to reflect onset of intrinsic excitation of charge carriers. However, in lack of further detailed and more accurate studies, we extract single activation energies over the measured temperature interval and obtain 0.4 ± 0.1 eV and 1.1± 0.2 eV for the series and parallel resistances, respectively. R_s is related to the resistance of the bulk materials and will be dominated by the component with the higher electrical resistance, in our case NiO. The observed activation energy of 0.4 eV is indeed close to literature values for NiO [31-33]. The activation energy of 1.1 ± 0.2 eV for the parallel shunt resistance R_p is much smaller than that of the saturation current density j_0, which was attributed to minority carrier diffusion and with an activation energy intermediate of the band gaps of the two materials ($E_{g,av}$ = 3.5 eV). We thus suggest that R_p may be related to mid-gap defect levels in the *p*–*n*-junction, as also suggested by Chavez *et al.* for Si-based junctions [34].

The built-in potential of a junction can be useful in the determination of the space charge distribution over the interface layer if the acceptor and donor densities are known [25]. It is related to the difference in the work functions (Ψ) of the materials, and with $\Psi_{NiO} \approx 5.4$ eV [35] and $\Psi_{ZnO} \approx 4.6$ eV [36], the theoretical total built-in potential of the junction is thus 0.8 eV. The total built-in potential of our *p*–*n* junction was obtained from capacitance-voltage (C–U_A) measurements at

900 °C. Linearization of C^{-2} vs U_A yielded a total built-in potential of 0.9 ± 0.1 eV from the bias voltage intercept, in good agreement with the theoretical value and close to potentials determined for NiO-ZnO systems by Grundmann *et al.*[24] around room temperature.

In the preceding treatment, we have applied voltages typical of biasing diodes and transistors in order to parameterize the current-voltage behavior of the *p*–*n*-junction. For thermoelectric applications, however, the voltage drop across the *p*–*n*-junction will have to be close to zero. Therefore, a practical parameter characterizing the junction is the area-specific open circuit resistance (R_0) near 0 V, i.e., the inverse slope of the j-U_A plot (*Figure 1) for* $U_A \rightarrow 0$ V. The obtained values are shown in *Figure 4* as a function of temperature. Similar to the series and parallel resistances reported in *Table 1*, also R_0 showed activated behavior, with an activation energy of about 1.0 ± 0.1 eV.

For thermoelectric applications, the R_0 of the junction must be small, typically in the order of 10^{-5} Ω cm^2 [37]. The R_0 measured for our *p*–*n*-junction is much larger, for example, around 60 Ω cm^2 at 600 °C, making this direct *p*–*n* junction unacceptable for most uses of TEGs. One way of reducing the R_0 is to corrugate the interface to increase the effective microscopic contact area per unit projected macroscopic area. A more efficient way should be to introduce a composite of the *p*- and *n*-type materials at the interface [38]. We demonstrate this by comparing j-U_A curves of two junctions with identical projected macroscopic cross-sections, but different interface morphologies. The first is a sample with the normal planar interface as described above and the other has a 50/50 mol% $Ni_{0.98}Li_{0.02}O$/$Zn_{0.98}Al_{0.02}O$ composite pellet inserted at the interface, forming what we refer to here as a *p*–*c*–*n* junction (top inset of *Figure 5*). The composite contains percolating paths of *p*-type and *n*-type conduction and hence serves to increase the effective area of *p*–*n*-junction.

Figure 5 illustrates that both junctions remained rectifying. For a given voltage, however, the current through the *p–c–n* sample was much higher than that through the planar *p–n* sample, and at 0 V (open circuit), composite reduced the resistance to approximately 1/6. Further reduction may be possible by using a finer microstructure of the composite component or developing self-assembled nanostructured interfaces [25]. Quantification of the effective interface area is difficult and outside the scope of the current proof-of-principle study. We note, however, that the average grain size of the components used here is much larger than the typical dimensions of space charge regions around the junction, so that the overall potential landscape remains unchanged.

While we have here demonstrated the working principle of an interface engineered junction using a large-grained composite, it is well worth investigating the influence of morphology on the electronic properties of the composite layer in the future, especially as grain sizes are reduced into the nanometer region corresponding to space charge layer and depletion zone thicknesses.

Conclusions

We have studied the characteristics of a heterojunction of polycrystalline $Ni_{0.98}Li_{0.02}O$ and $Zn_{0.98}Al_{0.02}O$ at high temperatures for possible application in high temperature electronics and with special attention to thermoelectric generators. The junction current-voltage characteristics exhibited rectification, which decreased by increasing temperature and were parameterized using the Shockley non-ideal diode model. From the extracted parameters, we suggest that minority carrier diffusion is the dominating contribution to the current under reverse bias. The calculated activation energies of the series and parallel shunt resistances were about 0.4 ± 0.1 eV and 1.1 ± 0.2 eV, respectively. The open circuit resistance R_0 of the junction, which determines the performance of the junction for thermoelectric generators, was for the direct normal *p–n* junction too large for practical applications. As a first proof-of-principle, the resistance was reduced by

almost an order of magnitude by increasing the effective area through utilization of a *p*–*n* composite at the interface.

Acknowledgements

The authors acknowledge the Research Council of Norway (RCN) for financial support under the THELMA project (228854) through the "Nano2021" program. We acknowledge A.E. Chatzitakis (Dept. Chemistry, Univ. Oslo) for support on the Mott-Schottky capacitance measurement and C. Zimmermann (Dept. Physics, Univ. Oslo) for writing the Python script for fitting to the Shockley diode model.

References

1. T. J. Seebeck, *Ann. Phys.* 1826, vol. 82, pp. 253-286.

2. G. J. Snyder and E. S. Toberer, *Nat. Mater.* 2008, vol. 7, pp. 105-114.

3. J. W. Fergus, *J. Eur. Ceram. Soc.* 2012, vol. 32, pp. 525-540.

4. G. Span, M. Wagner, T. Grasser and L. Holmgren, *Phys. Status Solidi-R* 2007, vol. 1, pp. 241-243.

5. A. Becker, R. Chavez, N. Petermann, G. Schierning and R. Schmechel, *J. Electron. Mater.* 2013, vol. 42, pp. 2297-2300.

6. W. Shin, N. Murayama, K. Ikeda and S. Sago, *J. Power Sources* 2001, vol. 103, pp. 80-85.

7. S. Woosuck, M. Norimitsu, I. Koichiro and S. Sumihito, *Jpn. J. Appl. Phys.* 2000, vol. 39, p. 1254.

8. S. Lany, J. Osorio-Guillén and A. Zunger, *Phys. Rev. B* 2007, vol. 75, p. 241203.

9. R. R. Heikes and W. D. Johnston, *J. Chem. Phys.* 1957, vol. 26, pp. 582-587.

10. M. Ohtaki, T. Tsubota, K. Eguchi and H. Arai, *J. Appl. Phys.* 1996, vol. 79, pp. 1816-1818.

11. M. Ohtaki, K. Araki and K. Yamamoto, *J. Electron. Mater.* 2009, vol. 38, pp. 1234-1238.

12. T. Tsubota, M. Ohtaki, K. Eguchi and H. Arai, *J. Mater. Chem.* 1997, vol. 7, pp. 85-90.

13. P. Jood, R. J. Mehta, Y. Zhang, G. Peleckis, X. Wang, R. W. Siegel, T. Borca-Tasciuc, S. X. Dou and G. Ramanath, *Nano Lett.* 2011, vol. 11, pp. 4337-4342.

14. Woosuck Shin and Norimitsu Murayama, *Jpn. J. Appl. Phys.* 1999, vol. 38, p. L1336.

15. W. Shin and N. Murayama, *Mater. Lett.* 2000, vol. 45, pp. 302-306.

16. C. H. Bates, W. B. White and R. Roy, *J. Inorg. Nucl. Chem.* 1966, vol. 28, pp. 397-405.

17. D.-S. Sinn, *Solid State Ionics* 1996, vol. 83, pp. 333-348.

18. T. D. Desissa, R. Haugsrud, K. Wiik and T. Norby, *Solid State Ionics* 2018, vol. 320, pp. 215-220.

19. B. Ifland, P. Peretzki, B. Kressdorf, P. Saring, A. Kelling, M. Seibt and C. Jooss, *Beilstein J. Nanotechnol.* 2015, vol. 6, pp. 1467-1484.

20. R. L. Anderson, *Solid State Electron.* 1962, vol. 5, pp. 341-351.

21. A. Cuevas, *Enrgy. Proced.* 2014, vol. 55, pp. 53-62.

22. C. Papadopoulos, In *Solid-State Electronic Devices: An Introduction,* (Springer New York: New York, NY, 2014), pp 11-80.

23. W. Shockley, *Bell Syst. Tech. J.* 1949, vol. 28, pp. 435-489.

24. M. Grundmann, R. Karsthof and H. von Wenckstern, *ACS Appl. Mater. Interfaces* 2014, vol. 6, pp. 14785-14789.

25. Z.-F. Shi, T.-T. Xu, D. Wu, Y.-T. Zhang, B.-L. Zhang, Y.-T. Tian, X.-J. Li and G.-T. Du, *Nanoscale* 2016, vol. 8, pp. 9997-10003.

26. D. Bozyigit, W. M. M. Lin, N. Yazdani, O. Yarema and V. Wood, *Nat. Commun.* 2015, vol. 6, p. 6180.

27. X. Yu, X. Shen, X. Mu, J. Zhang, B. Sun, L. Zeng, L. Yang, Y. Wu, H. He and D. Yang, *Sci. Rep.* 2015, vol. 5, p. 17371.

28. Z. Jin, A. Wang, Q. Zhou, Y. Wang and J. Wang, *Sci. Rep.* 2016, vol. 6, p. 37106.

29. G. Eneman, M. Wiot, A. Brugere, O. S. I. Casain, S. Sonde, D. P. Brunco, B. De Jaeger, A. Satta, G. Hellings and K. De Meyer, *IEEE Trans. Electron Devices* 2008, vol. 55, pp. 2287-2296.

30. C.-E. Sun, C.-Y. Chen, K.-L. Chu, Y.-S. Shen, C.-C. Lin and Y.-H. Wu, *ACS Appl. Mater. Interfaces* 2015, vol. 7, pp. 6383-6390.

31. J. Yu, K. M. Rosso and S. M. Bruemmer, *J. Phys. Chem. C* 2012, vol. 116, pp. 1948-1954.

32. J. G. Aiken and A. G. Jordan, *J. Phys. Chem. Solids* 1968, vol. 29, pp. 2153-2167.

33. M. B. Dutt, R. Banerjee and A. K. Barua, *Phys. stat. sol. (a)* 1981, vol. 65, pp. 365-370.

34. R. Chavez, S. Angst, J. Hall, F. Maculewicz, J. Stoetzel, H. Wiggers, L. T. Hung, N. V. Nong, N. Pryds, G. Span, D. E. Wolf, R. Schmechel and G. Schierning, *J. Phys. D: Appl. Phys.* 2018, vol. 51, p. 014005.

35. U. Kwon, B.-G. Kim, D. C. Nguyen, J.-H. Park, N. Y. Ha, S.-J. Kim, S. H. Ko, S. Lee, D. Lee and H. J. Park, *Sci. Rep.* 2016, vol. 6, p. 30759.

36. H. Moormann, D. Kohl and G. Heiland, *Surf. Sci.* 1979, vol. 80, pp. 261-264.

37. H. J. Goldsmid, In *Introduction to Thermoelectricity*, (Springer Berlin Heidelberg: Berlin, Heidelberg, 2016), pp 197-220.

38. R. Chavez, S. Angst, J. Hall, J. Stoetzel, V. Kessler, L. Bitzer, F. Maculewicz, N. Benson, H. Wiggers, D. Wolf, G. Schierning and R. Schmechel, *J. Electron. Mater.* 2014, vol. 43, pp. 2376-2383.

Figure captions

Figure 1. Current density-voltage (j-U_A) characteristics of $Ni_{0.98}Li_{0.02}O$–$Zn_{0.98}Al_{0.02}O$ heterojunction at 500 – 1000 °C. Dashed lines indicate fitting to experimental data. The inset shows a schematic of an equivalent circuit of the p-n heterojunction.

Figure 2. Arrhenius plot of the product of the extracted non-ideality factor and logarithm of saturation current density with the dashed line showing a linear fit the experimental data.

Figure 3. Arrhenius plot of the two extracted series and parallel resistances, R_s and R_p of the junction. The dashed lines are the linear fits to the experimental data.

Figure 4. R_0 calculated from the current-voltage curve at 0 V within the measurement temperature range of 600 – 1000 °C. The dashed line is the linear fit, whereas the error bars are the associated standard errors from linearization in the low voltage region.

Figure 5. j-U_A curves of $Ni_{0.98}Li_{0.02}O$ – $Zn_{0.98}Al_{0.02}O$ p–n junction at 500 °C of two junctions with different interface morphologies. The upper inset shows micrograph of the materials forming the p–c–n junction (the scale bar is representing the three microstructures), while the lower inset exhibits micrograph of the p–n junction sample.

Figure 1

Click here to download Figure Fig. 1.png

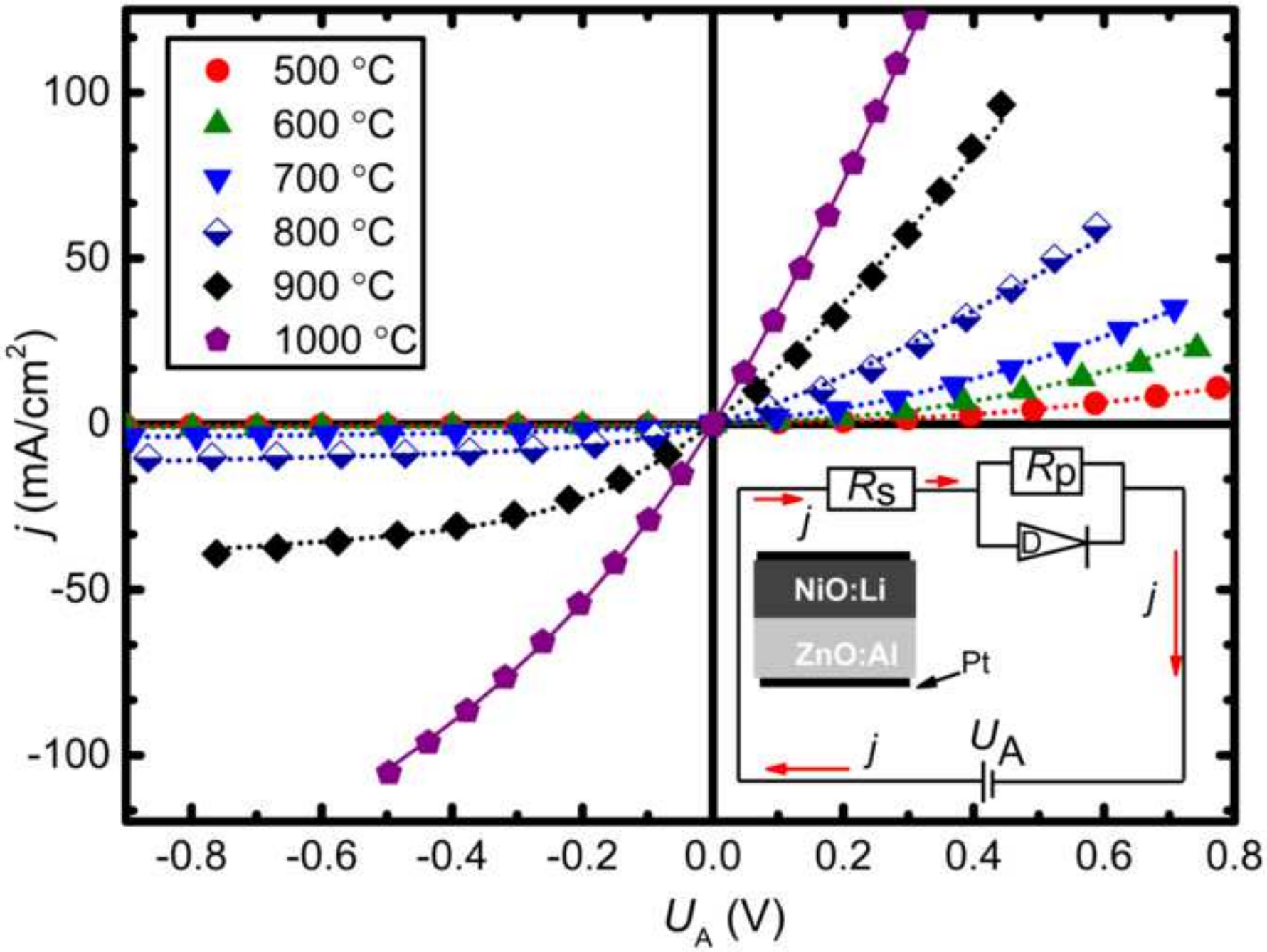

Figure 2

Click here to download Figure Fig. 2.png

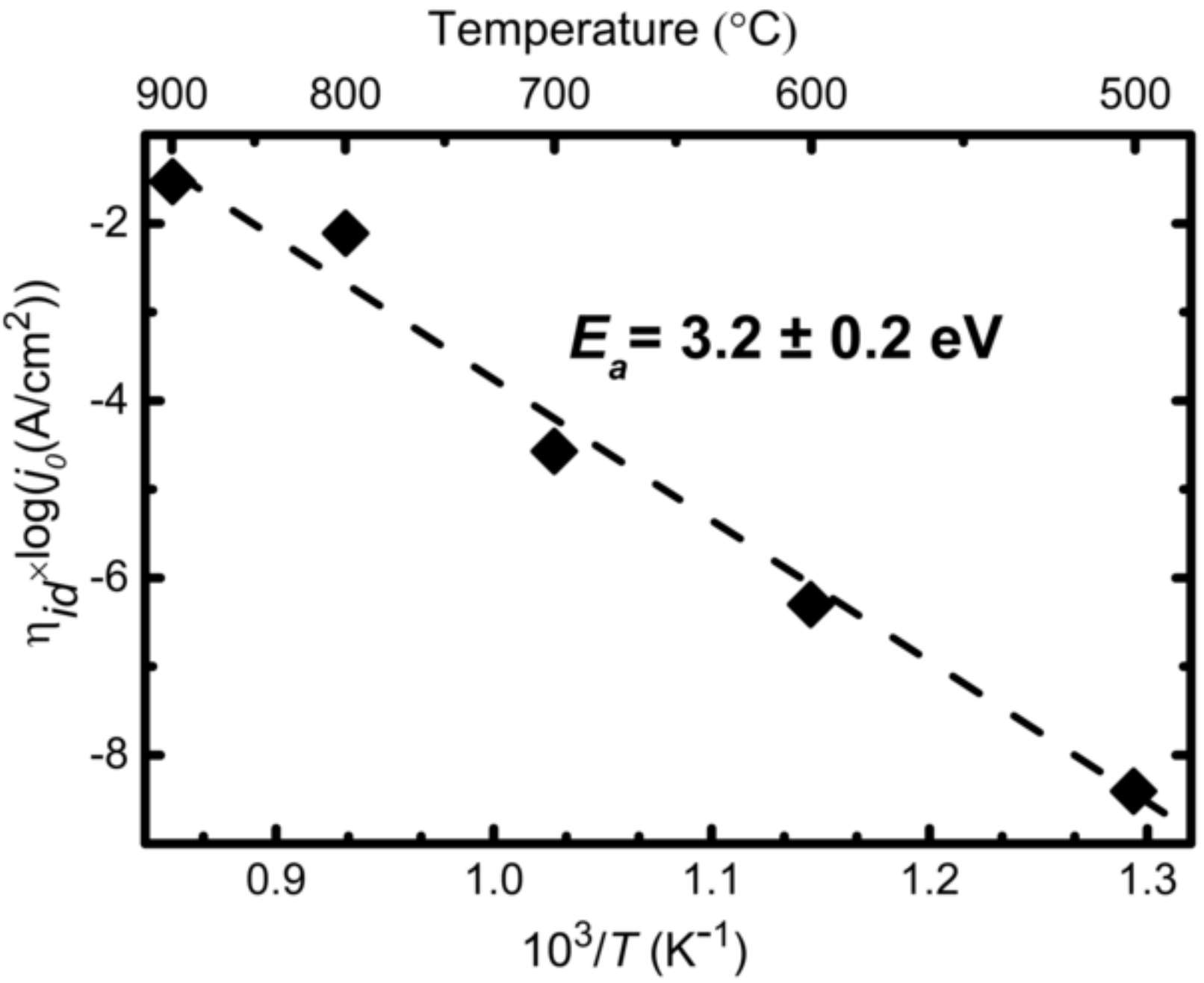

Figure 3

Click here to download Figure Fig. 3.png

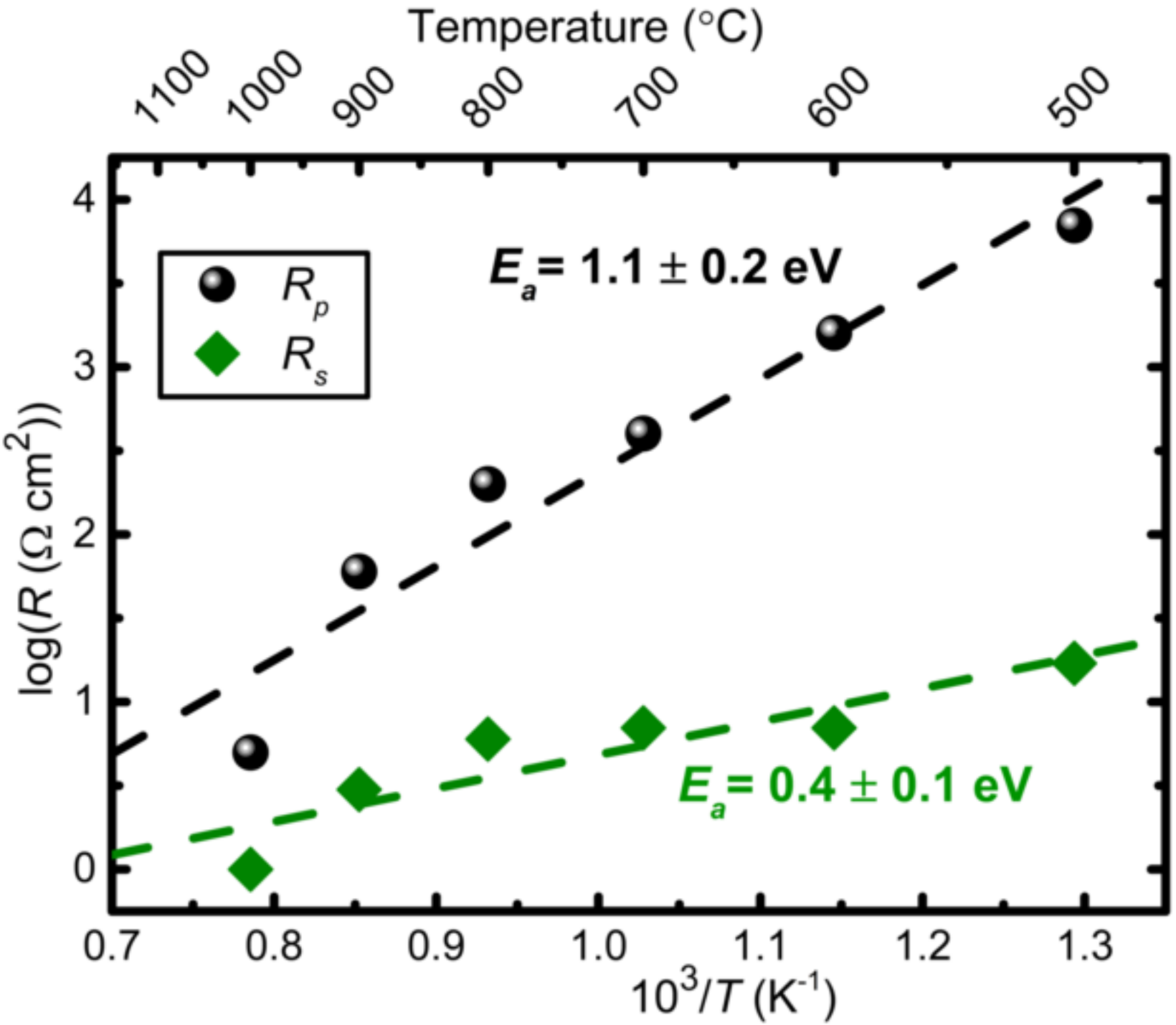

Figure 4

Click here to download Figure Fig. 4.png

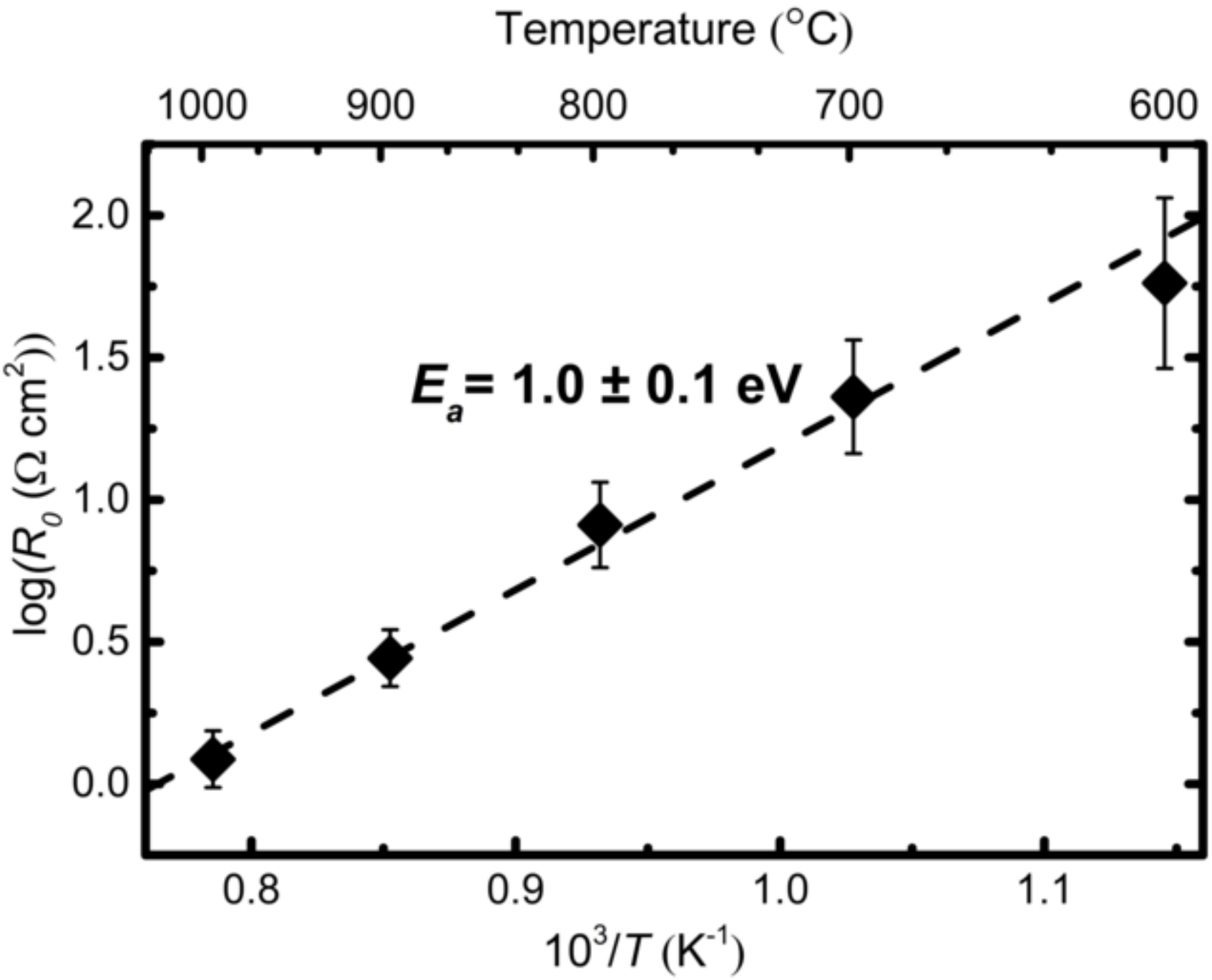

Figure 5

Click here to download Figure Fig. 5.png

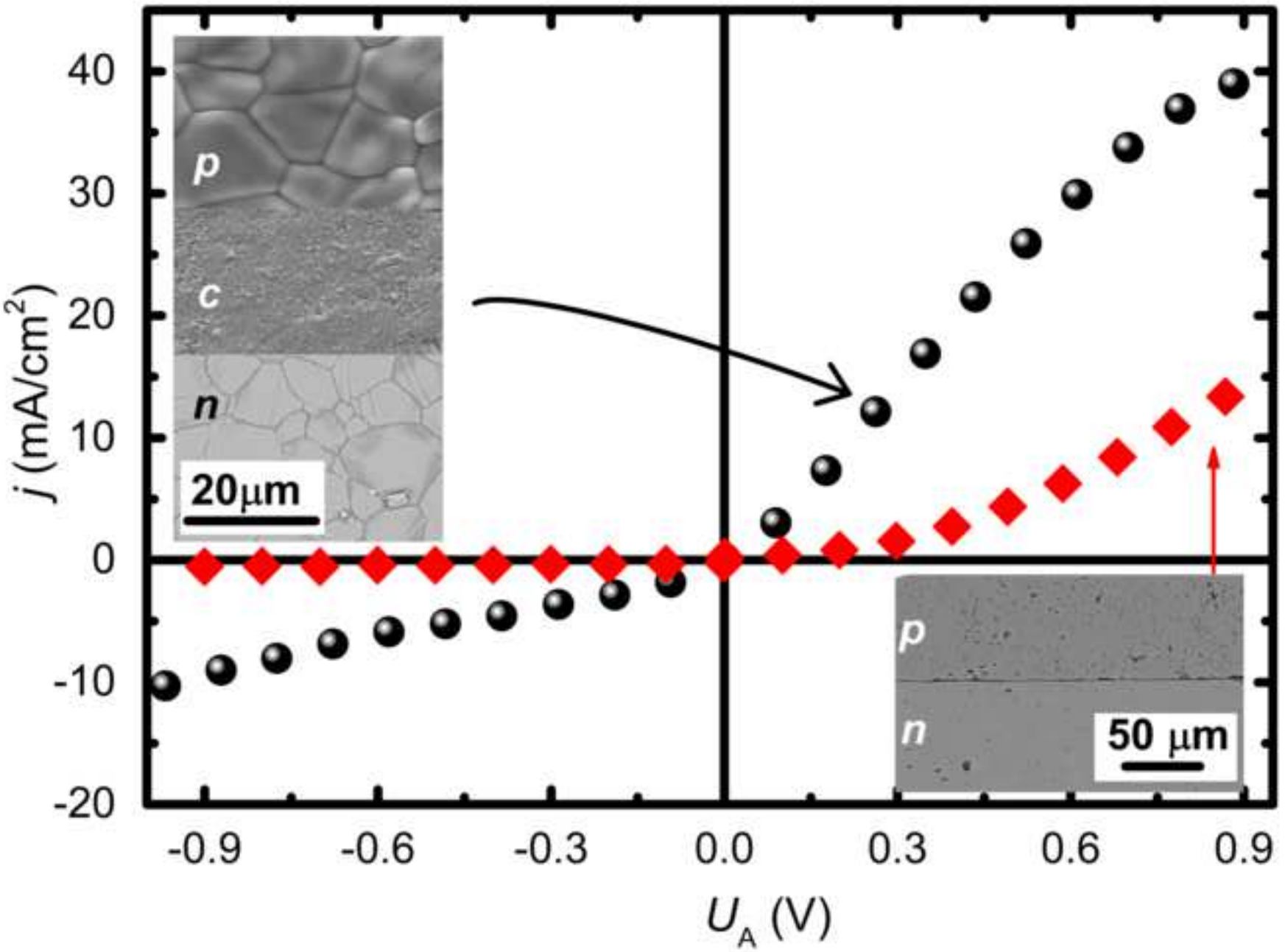

Table I. Parameters extracted from fitting of the experimental j-U_A curves in the temperature range 500 – 1000 °C.

Temperature (°C)	**Non-ideality factor, η_{id}**	**Saturation current density, j_0 (mA/cm^2)**	**R_s (Ω cm^2)**	**R_p (Ω cm^2)**
500	2.5	0.5	17	7000
600	2.0	1	7	1600
700	1.7	2	7	400
800	1.0	8	6	200
900	1.0	30	3	60
1000	1.0	-	1	5